Available online at www.sciencedirect.com
SCIENCE DIRECT
Thin-Walled Structures 43 (2005) 647–664
THIN-WALLED STRUCTURES
www.elsevier.com/locate/tws

Inward inversion of capped-end frusta as impact energy absorbers

A.A.N. Aljawi*, A.A.A. Alghamdi, T.M.N. Abu-Mansour, M. Akyurt

Department of Mechanical Engineering, King Abdulaziz University, P.O. Box 80204, Jeddah 21978, Saudi Arabia

Received 14 October 2003; accepted 26 July 2004
Available online 20 December 2004

Abstract

Results of an experimental investigation on the quasi-static axial inward inversion of right circular frusta are given. Effects of wall thickness, frustum angle and material on inversion were studied by quasi-static as well as drop hammer dynamic tests. Finite element (FE) modeling and analysis of the deformation modes are presented. The results of the experimental and the FE analyses are discussed. A good agreement is reported between the force histories predicted by the FE study and the experimental results.

Keywords: Energy absorber; Frusta inversion; ABAQUS

1. Introduction

Plastic energy absorbers are systems which possess the capacity to convert kinetic energy into permanent deformation in thin collapsible structures. The absorbed energy is irreversible and its magnitude depends on the material and shape of the absorber, loading rate and deformation pattern of the absorber [1].

One of the main functions of the absorber is to reduce the risk of injury or damage by controlling the deceleration pulse during impact. This is achieved by extending the period

* Corresponding author.
E-mail addresses: azhari_n@hotmail.com (A.A.N. Aljawi), aljinaidi@hotmail.com (A.A.A. Alghamdi), tabumansour@hotmail.com (T.M.N. Abu-Mansour), akyurt99@hotmail.com (M. Akyurt).

0263-8231/$ - see front matter
doi:10.1016/j.tws.2004.07.002

of dissipation of the kinetic energy of the system over a finite period of time. Cushioning devices on vehicle bumpers, crash retards in emergency systems of lifts and crash barriers used, as roadblocks are everyday examples.

The geometrical shape of collapsible energy absorbers can be circular [2], square [3], multicorner [4] and frusta [5]. Frusta are employed over a wide range of applications, especially in the domains of aerospace and armaments. Common examples occur in the nose cones of missiles and aircraft.

The plastic deformations in tubular structures are generally attributed to either lateral or/and axial loading. Investigations often lead to accounting for geometrical changes, interactions between modes of collapse, strain hardening and strain rate effects. Johnson and Reid [6] identified the dominant modes of deformation in simple structural elements in the form of circular and hexagonal cross-section tubes when these elements were subjected to various forms of quasi-static loading. They described the load–deformation characteristics of a number of these elements.

Thin-walled absorbers having symmetrical cross-sections may collapse in concertina or diamond mode or a mixture of both when subjected to axial loads [2]. The collapse of such components by splitting [7] or by inversion [8] is also reported.

The behavior of axially loaded thin tubes (large diameter to thickness ratio) has been of particular interest since the pioneering works of Alexander [2]. Circular tubes under axial compression are reported to be one of the most prevalent components in energy absorber systems [2]. In comparing lateral with axial compression, the axial mode has a specific energy absorbing capacity, which is approximately 10 times that of the same tube when compressed laterally between flat plates [1].

Postlethwaite and Mills [5] used Alexander's extensible collapse analysis to predict the mean crushing force for the concertina mode of deformation for frusta made of mild steel.

Mamalis and Johnson [9] investigated experimentally the crumbling of aluminum frusta subjected to axial compression load under quasi-static conditions. They proposed empirical relationships for both the concertina and the diamond modes of deformation. Mamalis et al. [10] extended their experimental study to include mild steel at elevated strain rates and concluded that the deformation modes of frusta could be classified as (a) concertina, (b) concertina-diamond, and (c) diamond. Mamalis and associates [11] produced a refined model of Postlethwaite and Mills [5] and obtained a better prediction for the mean crushing load. In another paper, Mamalis and his group [12] modeled the progressive extensible collapse of frusta and gave a theoretical model that depicts the changes in peaks and troughs of the experimental load–displacement curves. The comparison with the experimental results gave a fair degree of accuracy.

Extensive experimental studies were reported on the performance of compressed frusta subjected to quasi-static and dynamic axial loadings by Alghamdi [13], Aljawi and Alghamdi [14], Aljawi and Alghamdi [15], Alghamdi et al. [16,17] and by El-Sobky et al. [18]. Gupta and Abbas [19] presented a mathematical procedure for the calculation of the variation of crushing load for the axisymmetric axial crushing of thin frusta.

The above studies on frusta deal with axial crushing (or crumbling) of frusta between two parallel plates. A new mode of axial deformation of frusta was reported by Alghamdi [13] and Aljawi and Alghamdi [15]. This mode comprises of inward (outside-in, free or direct) inversion. In what follows, the authors' results are presented for experimental and finite element modeling studies conducted on the inward inversion of capped-end frusta.

2. Experimental

Table 1 summarizes the physical dimensions and masses of the frusta that were manufactured and tested. Most of the specimens were manufactured by manual spinning from 1050P blanks of commercial aluminum alloy sheets with size of 1.0 m in width and 2.0 m in length and few were made of mild steel and nylon plastic. The blanks were 1.0, 1.5, 2.0, 2.5, and 3.0 mm in thickness, and the frusta had the angles shown in Table 1. These frusta were inverted at quasi-static condition by the use of a 10-ton Instron universal testing machine (UTM), at a constant crosshead speed of 10 mm/min. Other specimens were inverted using a free-falling drop hammer facility (DHF) of 6.0 m maximum drop height, and a free-falling hammerhead of up to 6.9 kg.

A special jig consisting of an inversion rod, locating rings, and a base cylinder, was manufactured for the inversion process (see Fig. 1). The upper jaw of the UTM held the inversion rod, whereas the base rested on the lower jaw. The same jig was utilized with the DHF, in which case the inversion rod was simply attached to the falling weight.

3. Finite element modeling

The finite element method (FEM) has been used extensively to simulate applications in structural dynamics [20–23]. In the present study, the ABAQUS (explicit and implicit) code (version 5.8) was used to investigate the inversion of frusta under quasi-static and dynamic loading conditions [24].

A two-dimensional axisymmetric discretized FE model, shown in Fig. 1, was considered. The model, which represents a frustum loaded axially, consists of four parts. These are the frustum, rigid surfaces, representing the inversion rod and locating rings, a mass element, representing the hammer striker, and a contact link that allows the energy to be transferred from the striker to the frustum using the surface interaction. For the quasi-static case no mass was considered for the striker. Due to symmetry, half of the frustum was utilized for mesh generation (Fig. 1). Four-nodded axisymmetric continuum elements, suitable for large deformation plasticity, were used. To this end, CAX4R was selected for the explicit analysis, and CAX4 for the implicit analysis. Rigid bodies representing the inversion rod and the locating ring were modeled with two-nodded rigid elements (RAX2). In order to prevent sliding at the proximal ends, a coefficient of friction of $\mu = 0.3$ was incorporated between the rigid body surface and the upper small cap, and a value of 0.1 was assumed for the lower edge of the frustum. The number of elements ranged from 100 to 120 along the side and the upper small-capped-end of the frustum. Three elements were selected across the thickness. The particular number of elements along the side and the upper small cap was selected based on the mesh analysis size.

Table 1
Geometric and physical properties

Specimen no.	D (mm)	d (mm)	α (°)	t (mm)	h (mm)	L (mm)	H/t	L/t	M (g)	P_{avg} (N)	E (J)	Sp. E (J/g)
30102	72.04	24.52	30	1	15.8	24.8	15.8	24.8	12.212	712.7	17.68	1.448
30152	72.26	25.56	30	1.4	15.5	22.8	11.07	16.29	16.95	1214	27.68	1.633
30202	72.94	26.32	30	2	16.4	22.4	8.2	11.2	24.464	2231	49.98	2.043
30252	73	27.64	30	2.6	15.6	23.2	6.	8.92	29.951	2754	63.89	2.133
30302	71.22	28	30	3	16.74	25.6	5.58	8.53	34.205	4167	106.7	3.119
35102	69.74	23.22	35	1	16.22	29	16.22	29.0	11.841	895.0	25.96	2.192
35152	69.56	24.14	35	1.4	17.3	28	14.43	20.0	15.944	1497	41.94	2.631
35202	69.48	25.62	35	2	17.4	24	8.7	12.0	22.143	2612	62.69	2.831
35252	73	26.26	35	2.6	18.9	27.2	7.27	10.46	31.889	3437	93.49	2.932
35302	71	27.26	35	3	21	34	7.	11.33	35.991	5113	173.9	4.832
40102	72	22.66	40	1	21.32	34.8	21.32	34.8	13.537	933.1	32.47	2.399
40152	73	23.46	40	1.3	22.22	34.8	16.32	26.8	18.057	1564	54.42	3.014
40202	72.98	24.54	40	1.9	21.44	32.8	11.28	17.3	25.804	2869	94.10	3.647
40252	71.1	25.78	40	2.4	21.58	35.4	8.99	14.75	30.023	4381	155.1	5.165
40302	73.24	26.34	40	3.1	19.32	25.2	6.23	8.13	38.626	4458	112.3	3.4232
45102	71.6	22.64	45	1	24.66	44.5	24.66	44.5	14.222	1109	49.36	3.471
45152	71.78	23.8	45	1.4	25.72	43.5	18.37	31.07	19.37	1847	80.33	4.147
45202	72.4	24.76	45	1.9	25.5	43.5	13.42	22.89	27.408	3647	158.6	5.788
45252	73.2	25.28	45	2.4	26.02	42.5	10.84	17.71	34.385	4397	186.9	5.435
45302	75.5	26.52	45	2.9	27.6	46.5	9.52	16.03	44.202	5675	263.9	5.970
50102	70.5	22.46	50	0.9	29.9	54.5	32.22	60.56	14.53	1175	64.03	4.406
50152	71.88	23.26	50	1.2	30.54	53.5	25.45	44.58	19.737	2016	107.8	5.462
50202	71.2	24.46	50	1.8	31.32	53.	17.4	29.4	27.601	3596	192.1	6.960
50252	73.4	26.38	50	2.2	32.48	52.	14.76	23.64	36.558	4901	259.7	7.105
50302	74.92	26.94	50	2.8	33.24	–	11.87	–	47.13	–	Stopped	–
55102	71.46	22.98	55	0.9	36.84	64.5	40.93	71.67	16.085	1247	80.40	4.999
55152	72.7	23.9	55	1.3	36.04	68.	27.72	52.31	22.647	2151	148.2	6.543
55202	72.4	24.9	55	1.8	36.44	64.	20.24	35.56	32.152	3732	238.8	7.429
55252	73.94	25.42	55	2.1	38.3	69.	18.24	32.86	40.123	5659	390.5	9.732
55302	75.4	26.82	55	2.7	37.06	66.5	13.73	24.63	49.297	7241	481.5	9.767

60102	72.4	23.04	60	0.9	39	83.7	43.33	93.0	17.504	1160	97.12	5.549
60152	72.46	24.08	60	1.1	44	83.1	40.0	75.55	23.551	2200	182.8	7.762
60202	73.72	25.28	60	1.6	45.64	83.7	28.53	52.31	33.289	4107	343.8	10.33
60252	75	26.24	60	2	46.7	84.5	23.35	42.25	43.444	5854	494.7	11.39
60302	76.48	27.6	60	2.4	47.2	86.9	19.67	36.21	54.78	7161	622.3	11.36
65105	72.00	23.00	65	0.8	53.3	114	66.63	142.5	19.00	1419	147.7	7.774
65152	72.48	23.22	65	1.1	54.58	104.3	49.62	94.81	26.237	2446	255.1	9.723
65202	71.88	24.62	65	1.5	54.5	104	36.22	69.33	34.734	4029	419.0	12.06
65252	75	25.5	65	1.9	55.54	103.4	29.23	54.42	49.009	6159	636.8	12.99
65302	73.8	26.58	65	2.2	56.3	103.8	25.59	47.18	55.598	7586	787.4	14.162
70102	72.5	22.4	70	0.7	69	134.	98.57	191.4	21.696	1473	197.4	9.098
70152	72.49	23.2	70	1	68.86	128.	68.86	128.	28.552	2274	291.0	10.19
70202	72.78	24	70	1.4	68.16	–	48.69	–	40.119	–	Stopped	–
75102	71.4	22.56	75	0.7	93.54	–	133.63	–	27.808	–	Stopped	–
75152	72.56	23.2	75	1	94.42	165.7	94.52	165.7	37.543	2482	411.2	10.95
75202	73.24	24.4	75	1.3	94.34	–	72.57	–	50.285	–	Stopped	–
P30	75.00	20.00	30	2	15.88	31.77	7.940	15.88	15.412	1658	43.12	2.798
P45	75.00	20.00	45	2	27.50	38.89	13.75	19.45	18.786	3560	178.7	9.512
P60	75.00	20.00	60	2	47.63	55.00	23.82	27.50	26.436	4718	424.6	16.06
St30	75.00	20.00	30	1	15.88	31.77	15.88	31.77	36.823	3697	232.9	6.325
St45	75.00	20.00	45	1	27.50	38.89	27.50	38.89	39.185	5396	259.0	6.610
St60	75.00	20.00	60	1	47.63	55.00	47.63	55.00	59.762	9618	769.5	12.88

D, large diameter; *d*, small diameter; *h*, axial length; *t*, wall thickness; *m*, mass (g); α, angle of the frusta; P_{avg}, average load; *L*, max displacement; Eng, energy/g.

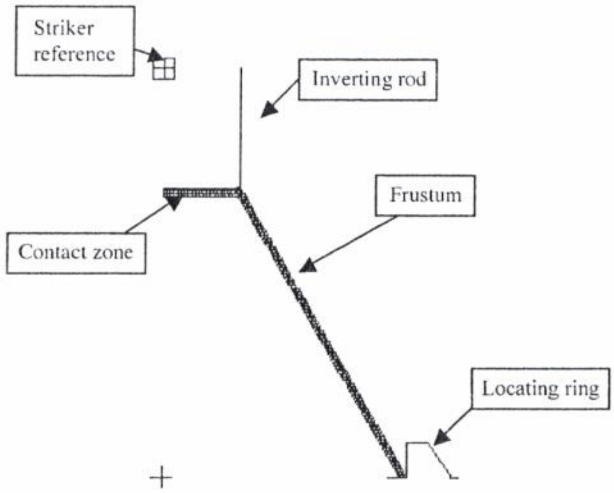

Fig. 1. Discretized 2-D axisymmetric FE model for direct inversion.

Material properties of the model were taken as rigid perfectly plastic, with yield strength (σ_y) of 125 MPa, mass density (ρ) of 2800 kg/m^3, Poisson's ratio (ν) of 0.33, and modulus of elasticity (E) of 69 GPa.

The boundary conditions imposed on the model were to constrain all the nodes on left side resembling plane of symmetry. The model is assumed to move only orthogonal to the model. The reference nodes located at the tip of the upper rigid body, the inversion rod; and on the lower rigid body, were also constrained. It is to be noted that the upper rigid body, shown in Fig. 1, can carry the relatively large mass element, representing the striker, and generates the impact loading of the frusta.

4. Results and discussion

Fig. 2 shows an experimental load–displacement curve for specimen no. 40102, having a semi-apical angle of 50°. The behaviors of other specimens were similar. It is obvious that the deformation passes through a number of stages. In the first stage, the load rises quasi-linearly from the origin until it reaches its initial maximum instability load (P_{imax}), where a circular plastic zone forms, point a in Fig. 2. The load, afterwards, decreases smoothly to a certain extent, until it reaches its first minimum load, P_{imin}, point b. The zone between a and b is a zone of incubation, within which the cap of the frustum is deformed in such a manner as to facilitate the inversion type of deformation. Two localized plastic zones are developed from point a to b on P–δ curve shown in Fig. 2, and an extensible mode of deformation is observed.

As the load continues, the plastic zone extends towards the larger (lower) end of the frustum, until point c is reached (see Fig. 2). The increase in the inversion force from b to c is attributed to the progressive increase in the volume of the deformation zone with the increasing D/t ratio.

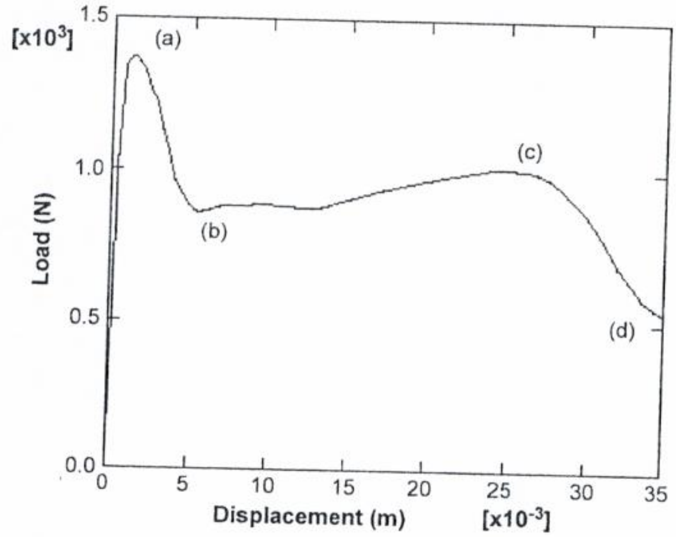

Fig. 2. Load–displacement curve for capped aluminum frustum direct inversion, specimen no. 40102, at $\alpha=40°$, large diameter, $D=72.0$ mm, small diameter, $d=22.66$ mm, and height, $h=21.32$ mm.

Point c signals the termination of the inversion zone, the bending front having reached the vicinity of the free large end of the frustum. From point c to d inversion mode changes into a flattening mode, and the undeformed part of the frustum has the shape of a Belleville spring. The free end of the frustum is flattened parallel to the shoulder of the jig base. A typical image of the direct inversion of capped aluminum frustum in the region between b and c of specimen no. 65252 is shown in Fig. 3.

Samples of load–displacement curves for specimens listed in Table 1 are shown in Figs. 4 and 5. Fig. 4 shows the load–displacement curves of aluminum frusta of similar thickness ($t=1$ mm) but of different apical angles. The performances of these specimens are identical, but the displacement increases with the increase in the angle. However, deformation pattern of frusta with large angles ($\alpha=70$ and $75°$) includes extensible collapse mode of deformation [10]. This could be the reason for not being able to invert frusta with the larger angles presented in Table 1.

Load–displacement curves of frusta with different thicknesses and at similar angles ($\alpha=30°$) are presented in Fig. 5. It is obvious that the deformation pattern is repeated and the average inversion force increases as the frusta become thicker. Identical frusta having the same geometry but made of different materials were subjected to inversion loading. As is expected, low-carbon steel absorb more energy during inversion than that made of either nylon plastic or frusta made of aluminum. The progress of deformation of a frustum (specimen P60) is captured in Fig. 6.

From these figures, it can be observed that the load–displacement curves of all frusta closely follow the four stages of deformation mode explained earlier, and that the load increases with the increase in wall thickness for frusta with different angles. This increase becomes very substantial in frusta of larger wall thicknesses and larger angles. However,

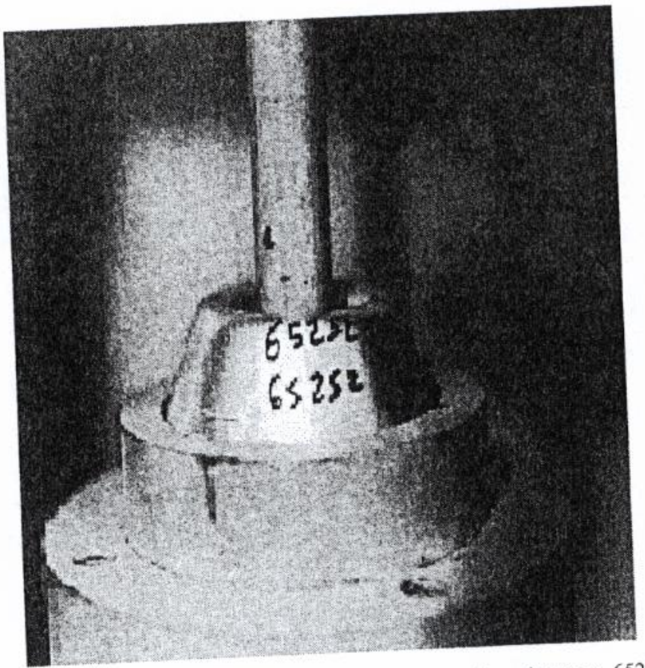

Fig. 3. Direct inversion of capped aluminum frustum of specimen no. 65252.

the mode of collapse (complete inward inversion of the upper end of frusta) is not affected by the wall thickness and the apical angle.

Variations in load–displacement curves may be attributed to the nonuniformity in the wall thickness of the loaded frusta. These differences arise due to the spinning process.

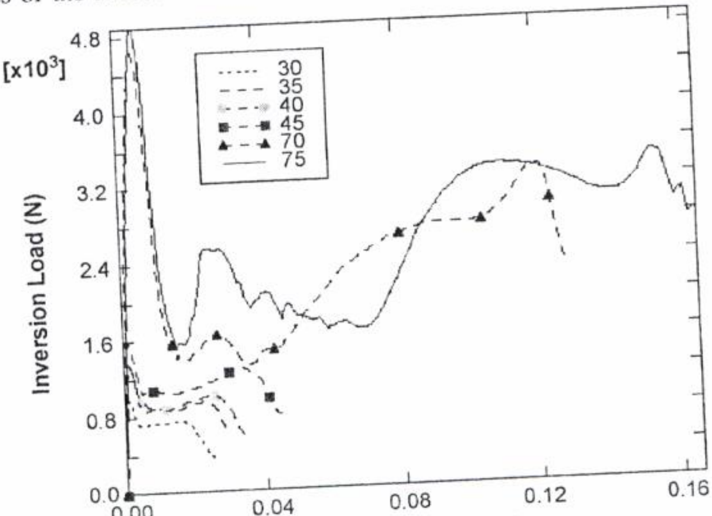

Fig. 4. Experimental quasi-static load–displacement curves of aluminum frusta for different angles α of; 30, 35, 40, 45, 70, and 75°, and nominal thickness of 1 mm.

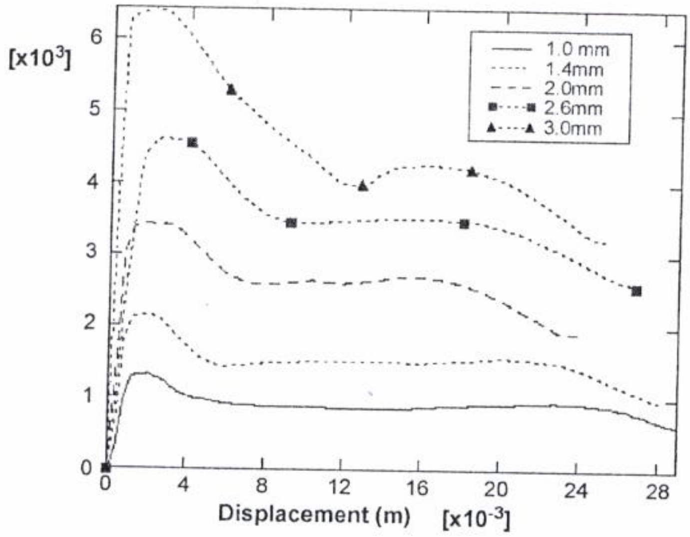

Fig. 5. Experimental quasi-static load–displacement curves of aluminum frusta for angles α of 35°, and different thickness.

As may be expected, the stroke length, i.e. the maximum displacement achieved by the inversion process, increases with increasing α since all specimens were fabricated such that they all have the same upper and lower diameters. However, for specimens 50302, 70202, 75102, and 75202, this stroke was not completed, as the frusta collapsed by rupture at the leading edge of the smaller diameter before the completion of inversion.

The average load and specific energy dissipated during plastic deformation throughout the inversion process are summarized in Table 1. The range of h/t ratio varies from 5 to

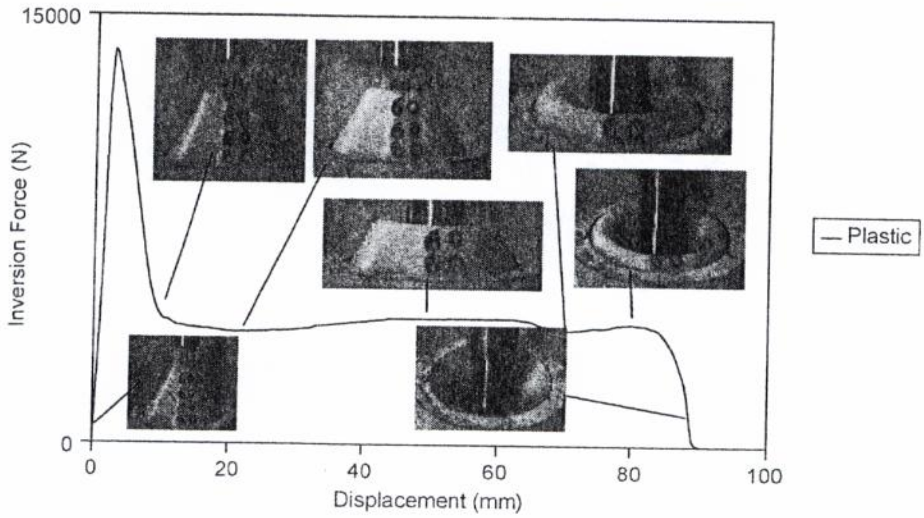

Fig. 6. Experimental deformed plots for inward inversion of specimen P60 frustum captured at 0, 10, 20, 50, 70, 80, and 90 mm, respectively.

134 for angles ranging from 30 to 75°. It may be verified that the average load increases, nearly linearly, with increasing angle of frustum. For high values of h/t (thin and long frusta), the specific energy is low when compared with that of low values of h/t.

Only the load–displacement curves for plastic frusta made by machining are listed in Table 1. It is clear that load–displacement curves for frusta made from plastic materials are similar to those obtained by aluminum frusta.

The possibility of re-using the inverted frusta was also investigated. Several tests were conducted for inversion and then re-inversion of the inverted frusta. Fig. 7 shows the load–displacement curves for inversion and re-inversion of one specimen, indicating that it is possible to invert and re-invert the frustum of certain geometric proportions, but not all. This particular specimen failed, however, during its fourth inversion.

Fig. 8 shows experimental findings along with FE load–displacement predictions for specimens 35102 and 60102. It may be observed that there is generally good agreement between the experimental results and the FE predictions except at the beginning of inversion. The deviation occurs at the beginning of the first stage, where ABAQUS analysis starts at a large load, and decreases to the point of the elastic recoverable region. This sizable discrepancy is due to the fact that ABAQUS assumes that the plastic behavior of the material is described by its yield point, corresponding to zero initial plastic strain.

The experimentally measured specific energies absorbed during the inward inversion by specimens 35102 and 60102 were 2.192 and 5.549 J/g, whereas those predicted by FE were 2.55 and 6.07 J/g, respectively. The slight overshoot of the FE predictions may be attributed to the sudden increase of the load within the elastic phase.

Different stages of the inversion process, as predicted by the FE analysis, are presented in Fig. 9. It may be noted that the second and the sixth stages indicate the initiation and termination of the inversion process, respectively.

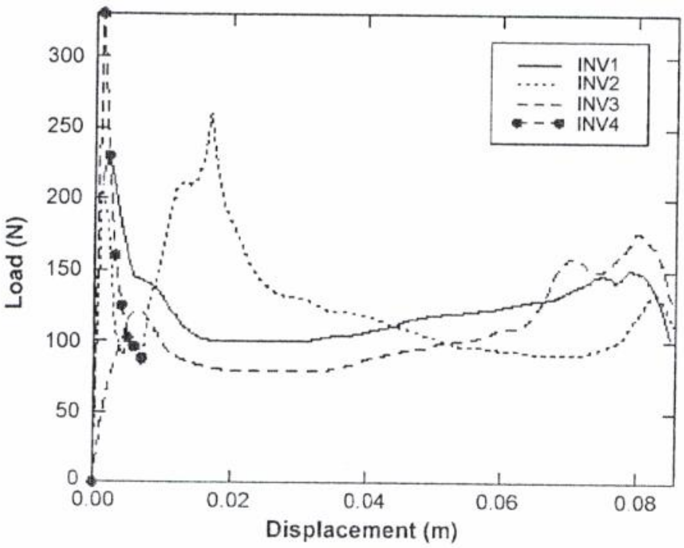

Fig. 7. Load–displacement curves for inversion and re-inversion of capped aluminum frusta.

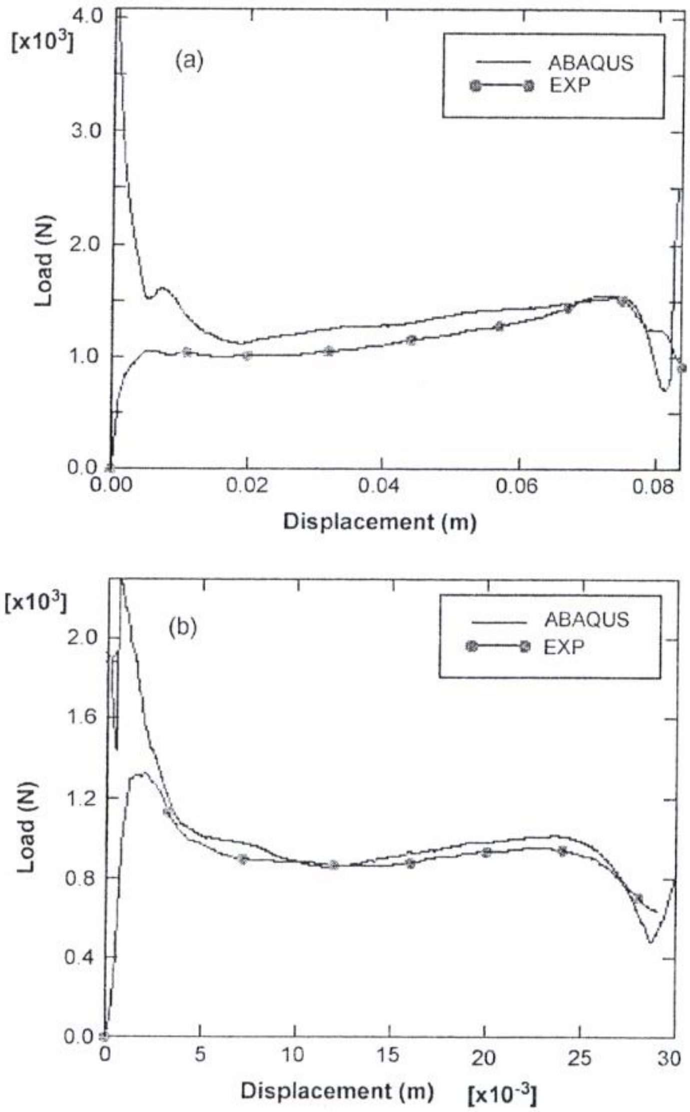

Fig. 8. Experimental and FE load–displacement curves for quasi-static inward inversion of capped aluminum frustum of specimens no. (a) 60102, and (b) 35102.

Fig. 10 shows a comparison between the deformed frusta produced by experiment and that predicted by FE. Here, a symmetrical half of the frustum is seen before and after the inversion, as predicted by the FE analysis as well as a photograph of the frustum. Excellent agreement can be observed between the two deformed shapes.

In order to assess the effect of speed on the process of inversion, identical frusta were tested using UTM at crosshead speeds of 2, 20 and 200 mm/min. Additional tests

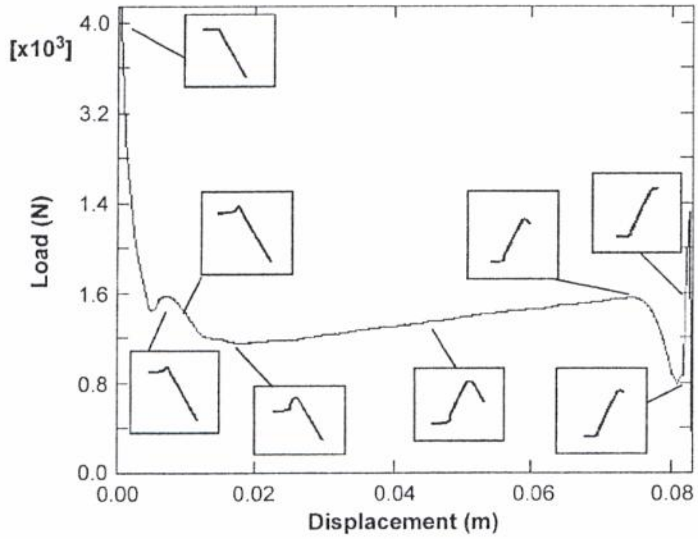

Fig. 9. ABAQUS deformed plots for inward inversion of capped aluminum frustum at eight different stages of deformation, at 0.4, 5.8, 7.1, 19.1, 54.9, 76.9, 81, and 82.5 mm, of specimen no. 60102.

were conducted on the DHF using different falling masses. Impact velocities of up to 7 m/s were used in these tests. Velocities were calculated using the relationship $V=\sqrt{2\times 9.81\times h}$ where h is the drop height. It was observed that all specimens in these tests showed similar behavior as in quasi-static tests. The geometric shapes of

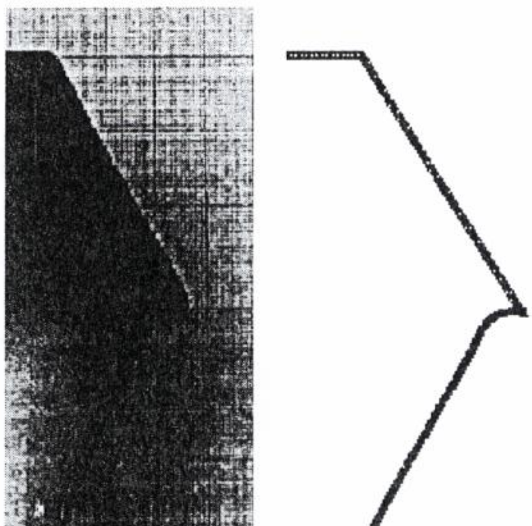

Fig. 10. Comparison between the experimental and finite element analysis of a frustum before and after inversion.

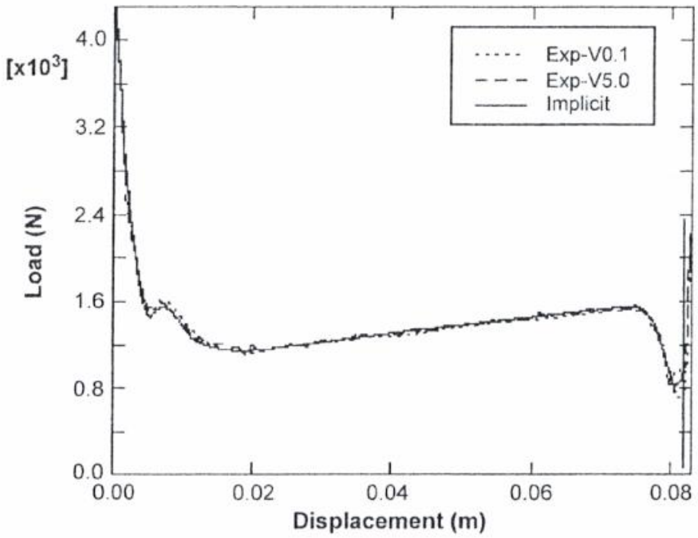

Fig. 11. Comparison between the explicit analysis at constant $v=0.1$, and 5.0 m/s, with the quasi-static implicit analysis for specimen no. 60102.

the frusta inverted under quasi-static condition were very similar to those inverted under dynamic conditions.

Since generally good agreement was obtained between experimental findings and FE predictions in quasi-static conditions, it was considered plausible to expect FE analysis to provide insight into inversion during the dynamic loading of frusta. To this end, a number of runs were made on the ABAQUS. Thus, Fig. 11 depicts the prediction of the effect of crosshead speeds on load–displacement curves. For the predictions, both the quasi-static implicit software and the dynamic explicit version were run at constant velocities of $v=0.1$ and 5.0 m/s, which correspond to 2.63 and 131.6 strain/s. It seems evident from Fig. 11 that the inversion process is not affected by the loading rate at low impact velocities.

For the high speed tests, a striker of mass 6.9 kg was assumed, and the impact velocities were in the range of 3–20 m/s. Results of the dynamic inversion testing are listed in Table 2, and depicted in Figs. 12 and 13. The results seem to indicate that increasing the impact velocity has no effect on the modes of deformation. In fact, complete inward inversion took place for striker velocities higher than 5.74 m/s, while the striker rebound when the velocities is equal or less than 5.74 m/s (see Fig. 13). It is interesting to note that, at zero rebound velocity, the striker will remain in contact with the fully inverted frustum.

Fig. 12 shows that for higher impact velocities, less time is required for complete inward inversion. Although, more kinetic energy is provided by the striker, the energy dissipated due to plastic deformation (or the average load) remains constant. The deformation is mostly dominated by bending, starting by hinge-rotation deformation at the leading edge of the upper cap and continues until a complete inversion of the frustum.

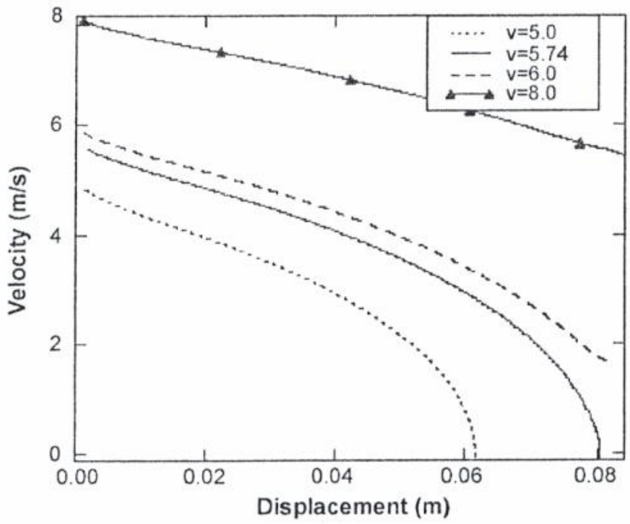

Fig. 13. Velocity–displacement curves due to dynamic impact of specimen 60102 with striker mass of 6.9 kg, and initial velocities, $v=5$, 5.74, 6 and 8 m/s.

for the strain rates to be both velocity and mass sensitive. The strain rate can be expressed by the Cowper–Symonds [25] empirical power law

$$\bar{\sigma}(\bar{\varepsilon}^p) = \sigma_s(\bar{\varepsilon}^p)\left[1 + \left(\frac{\dot{\bar{\varepsilon}}}{D}\right)^{\frac{1}{p}}\right]$$

where $\sigma_s(\bar{\varepsilon}^p)$ is the quasi-static yield stress, $\bar{\sigma}(\bar{\varepsilon}^p)$ denotes the dynamic yield stress, $\dot{\bar{\varepsilon}}$ is the strain rate, and D and p are material constants to be determined experimentally. The values

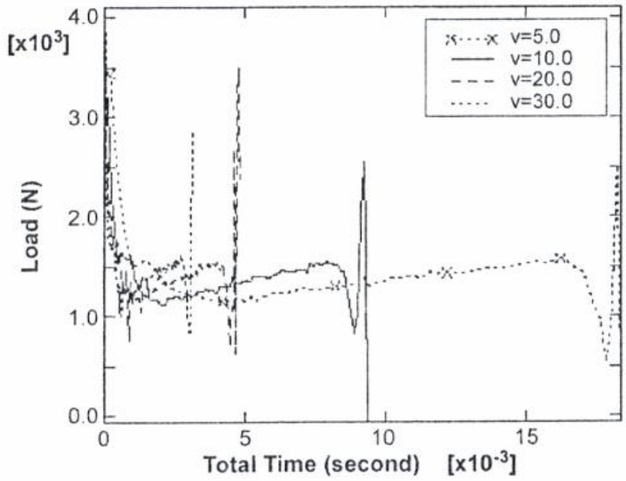

Fig. 14. Load–time curves due to dynamic impact energy of 345 J on specimen 60102 with different striker mass and velocity of: $v=5$ m/s and mass=27.6 kg, $v=10$ m/s and mass=6.9 kg, $v=20$ m/s and mass=1.725 kg, and $v=30$ m/s and mass=0.7667 kg.

Table 2
Results of dynamic impact loadings of specimen no. 60102

V_i (m/s)	Mass (kg)	V_t (m/s)	V_r (m/s)	t (ms)	E_{in} (J)	E_{pl} (J)	L (mm)	Modes of deformation
20.0	6.9	19.09	–	4.2924	1380.	114.6	83.8	CIWI
18.0	6.9	16.99	–	4.80	1117.8	114.3	83.9	CIWI
16.0	6.9	14.86	–	5.445	883.2	114.5	83.9	CIWI
14.0	6.9	12.72	–	6.2	676.2	111.8	82.6	CIWI
12.0	6.9	10.45	–	7.5	496.8	114.5	84.0	CIWI
10.0	6.9	8.114	–	9.24	345.0	113.3	83.4	CIWI
8.0	6.9	5.462	–	12.46	220.8	113.6	83.5	CIWI
6.0	6.9	1.61	–	22.0	124.2	111.7	82.2	CIWI
5.74	6.9	–	0.104	28.8	113.67	110.2	80.44	PIWI
5.0	6.9	–	0.147	25.8	86.25	83.5	61.3	PIWI
5.0	27.6	4.077	–	18.20	345.0	112.0	83.0	CIWI
20	1.725	16.11	–	4.656	345.0	114.2	83.67	CIWI
30	0.7667	23.98	–	3.10	345.0	114.0	83.11	CIWI

V_t, terminal velocity; V_r, rebound velocity; t, total time for the inversion or rebound; E_{in}, model input energy; E_{pl}, energy dissipated due to plastic deformation; L, length of the stroke; CIWI, complete inward inversion; PIWI, partial inward inversion.

Fig. 14 shows load variations with time when the frustum is subjected to identical impact energy of 345 J, resulting from different combinations of the striking mass and the initial velocities. Once more, it may be verified from Fig. 14 that the large mass and low velocities do not cause any effect on material behavior. In fact, more time is required to complete the inward inversion.

In dynamically loaded aluminum structures, high-velocity impacts may cause significant strain rates, especially during the initial stages of impact, and it is possible

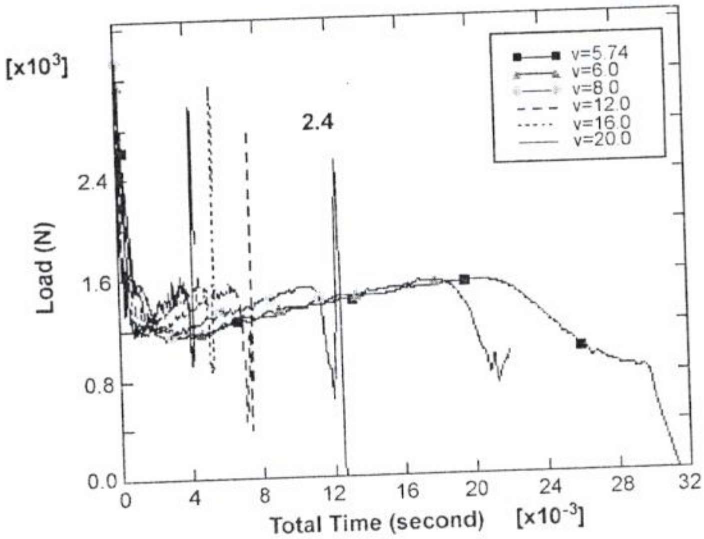

Fig. 12. Load–time curves due to dynamic impact of specimen 60102 with striker mass of 6.9 kg, and initial velocities, v=5.74, 6, 8, 12, 16, and 20 m/s.

complete inversion. When $m_s \gg m_f$, it follows that

$$\sum W_{1-2} \approx E_{pl} = -P_{avg}L \quad \text{and} \quad \int_{t1}^{t2} F\,dt \approx -P_{avg}t$$

where E_{pl} is the energy dissipated due to plastic deformation, P_{avg} is average load, and L is the stroke length, and t is the time required for complete inversion. Evaluating for quasi-static condition, the above expressions can be simplified to

$$V_t = \sqrt{\frac{m_s V_i^2 - 2E_{pl}}{m_s}} \quad \text{and} \quad t = \frac{m_s(V_i - V_t)}{P_{avg}} \tag{3}$$

$$\text{Note that for } V_t = 0 \text{ (No rebound)}, V_i = \sqrt{\frac{2E_{pl}}{m_s}} \text{ and } t = \frac{m_s(V_i)}{P_{avg}} \tag{4}$$

Thus taking specimen 60102 as an application, one finds that complete inversion occurs at L=83.2 mm, P_{avg}=1373 N, and E_{pl}=114.2 J. The minimum velocity of a striker of mass 6.9 kg becomes 5.753 m/s for complete inversion of the frustum without any rebound. The time required for inversion comes out to be 28.912 ms. It may be verified that these values are very close to the corresponding figures obtained by ABAQUS, as listed in Table 2.

6. Conclusions

The results of the experimental part of the investigation on the quasi-static axial inward inversion of right circular frusta indicate that the process of inversion follows a four-stage deformation mode. The load needed for inversion increases with increasing wall thickness and increasing frustum angle. For high values of height h to thickness t ratio, specific energy of deformation is less than that for lower values of h/t.

FE predictions of the deformation process are generally in good agreement with the experimental findings.

The process of inward inversion seems to be a new mode of deformation that is repeatable and predictable. Inversion of frusta is achieved by the use of a simple rig. In fact, it was found that a frustum can be inverted several times, indicating that it is possible to re-use the same absorber.

References

[1] Alghamdi AAA. Collapsible impact energy absorbers: an overview. Thin Wall Struct 2001;39:189–213.

[2] Alexander JM. An approximate analysis of the collapse of thin cylindrical shells under axial loading. Q J Mech Appl Math 1960;13:10–15.

[3] Abramowicz W, Jones N. Dynamic axial crushing of square tubes. Int J Impact Eng 1984;2(2):179–208.

[4] Wierzbicki T, Abramowicz W. On the crushing mechanics of thin-walled structures. J Appl Mech 1983; 50(4):727–34.

[5] Postlethwaite HE, Mills B. Use of collapsible structural elements as impact isolators with special reference to automotive applications. J Strain Anal 1970;5:58–73.

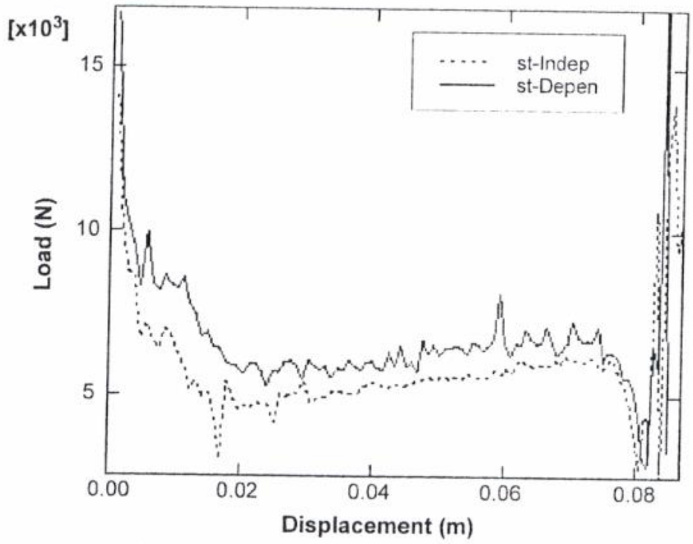

Fig. 15. Comparison of the load–displacement curves between the strain rate independent (...), and strain rate dependent (—) due to dynamic impact energy of 345 J on specimen 60102 at velocity of 20 m/s.

of $D=1{,}288{,}000\ \mathrm{s}^{-1}$ and $p=4$ are adopted for aluminum [23,26]. Using these properties, Fig. 15 shows the effect of strain rate on the load–displacement curves for a frustum identical to specimen 60102 at a velocity of 20 m/s and mass of 1.725 kg. An increase of the load, and consequently more energy is required for complete inversion. Note that the increase in the energy absorbed by the frustum due to strain-dependent does not change the mode of deformation, i.e. complete inward inversion.

5. Simplified analytical results

A simplified solution, based on data obtained from quasi-static loading conditions, can be obtained for yielding terminal velocities as well as the time required for complete inversion. Thus, considering the conditions of conservation of energy and of linear impulse and momentum

$$\frac{1}{2}m_s V_i^2 + \sum W_{1\text{-}2} = \frac{1}{2}(m_s + m_f)V_t^2 \tag{1}$$

$$m_s V_i + \int_{t1}^{t2} F\,\mathrm{d}t = (m_s + m_f)V_t \tag{2}$$

where m_s is the mass of the striker, V_i and V_t are the initial and terminal velocities of the striker, and m_f is the mass of the upper capped of the frustum. $\sum W_{1\text{-}2}$ is the work done during the inversion, and $\int_{t1}^{t2} F\,\mathrm{d}t$ is the impulse force applied during the time required for

[6] Johnson W, Reid SR. Metallic energy dissipating systems. Appl Mech Rev 1978;31:277–88.
[7] Stronge WJ, Yu TX. Long stroke energy dissipating in splitting tubes. Int J Mech Sci 1984;25:637–47.
[8] Al-Hassani STS, Johnson W, Lowe WT. Characteristics of inversion tubes under axial loading. J Mech Eng Sci 1972;14:370–81.
[9] Mamalis AG, Johnson W. The quasi-static crumpling of thin-walled circular cylinders and frusta under axial compression. Int J Mech Sci 1983;25:713–32.
[10] Mamalis AG, Johnson W, Vigilant GL. The crumbling of steel thin-walled tubes and frusta under axial compression at elevated strain-rate: some experimental results. Int J Mech Sci 1984:26:537–47.
[11] Mamalis AG, Manolakos DE, Saigal S, Viegelahn G, Johnson W. Extensible plastic collapse of thin-wall frusta as energy absorbers. Int J Mech Sci 1986;28:219–29.
[12] Mamalis AG, Manolakos DE, Viegelahn GL, Johnson W. The modeling of the progressive extensible plastic collapse of thin-wall shells. Int J Mech Sci 1988;30:249–61.
[13] Alghamdi AAA. Design of simple collapsible energy absorber. MSc thesis. College of engineering, Jeddah, Saudi Arabia: King Abdulaziz University; 1991.
[14] Aljawi AAN, Alghamdi AAA. Investigation of axially compressed frusta as impact energy absorbers. In: Gaul L, Brebbia AA, editors. Computational methods in contact mechanics IV. Southampton: WIT Press; 1999. p. 431–43.
[15] Aljawi AAN, Alghamdi AAA. Inversion of frusta as impact energy absorbers. In: Hassan MF, Megahed SM, editors. Current advances in mechanical design and production VII. New York: Pergamon Press; 2000. p. 511–9.
[16] Alghamdi AAA, Aljawi AAN, Abu-Mansour TMN, Mazi RAA. Axial crushing of frusta between two parallel plates. In: Zhao XL, Grzebieta RH, editors. Structural failure and plasticity. New York: Pergamon Press; 2000. p. 545–50.
[17] Alghamdi AAA, Aljawi AAN, Abu-Mansour TMN. Modes of axial collapse of unconstrained capped frusta. Int J Mech Sci 2002;44:1145–61.
[18] El-Sobky H, Singace AA, Petsios M. Mode of collapse and energy absorption characteristics of constrained frusta under axial impact loading. Int J Mech Sci 2001;43:743–57.
[19] Gupta NK, Abbas H. Axisymmetric axial crushing of thin frusta. Thin Wall Struct 2000;36:169–79.
[20] Bammann DJ, Chjiesa ML, Horstemeeyer MF, Weigaten LT. Failure in ductile materials using finite element methods. In: Jones N, Wierzbick T, editors. Structural crashworthiness and failure. London: Elsevier; 1993. p. 1–54.
[21] Kormi K, Shaghouei E, Duddell DA. Finite element examination of dynamic response of clamped beam grillages impacted transversely at their center by a rigid mass. Int J Impact Eng 1994;15:687–97.
[22] Aljawi AAN. Finite element and experimental analysis of axially compressed plastic tubes. Eur Soc Mech Environ Eng 2000;45(1):3–10.
[23] Karagiozova D, Alves M, Jones N. Inertia effects in axisymmetrically deformed cylindrical shells under axial impact. Int J Impact Eng 2000;24:1083–115.
[24] HKS, Inc, ABAQUS/Explicit user's manual, theory and examples manual and post manual, version 5.8; 1998.
[25] Symonds PS. Viscoplastic behavior in response of structures to dynamic loading. In: Huffington NJ, editor. Behaviour of materials under dynamic loading. New York: SME; 1965. p. 106–24.
[26] Jones N. Structural impact. Cambridge: University Press; 1989.